(2)

OFFICE OF NAVAL RESEARCH

CONTRACT N00014-84-k-0656/O00002

R & T Code 413d018

Technical Report #19

Probing Interfacial Structure and Composition with X-ray Standing Waves

Héctor D. Abruña and Michael J. Bedzyk*
Department of Chemistry, Baker Laboratory
*Cornell High Energy Synchrotron Source
and School of Applied & Eng. Physics
Cornell University
Ithaca, New York 14853

Prepared for Publication in
Accounts of Chemical Research
June 4, 1990

- UNCLASSIFIED

SECURITY CLASSIFICATION OF THIS PAGE

REPORT DOCUMENTATION PAGE

1a. REPORT SECURITY CLASSIFICATION unclassified	1b. RESTRICTIVE MARKINGS
2a. SECURITY CLASSIFICATION AUTHORITY unclassified	3. DISTRIBUTION / AVAILABILITY OF REPORT unlimited
2b. DECLASSIFICATION / DOWNGRADING SCHEDULE	
4. PERFORMING ORGANIZATION REPORT NUMBER(S) Technical report # 19	5. MONITORING ORGANIZATION REPORT NUMBER(S)
6a. NAME OF PERFORMING ORGANIZATION Hector D. Abruna Cornell University 6b. OFFICE SYMBOL (If applicable)	7a. NAME OF MONITORING ORGANIZATION Office of Naval Research
6c. ADDRESS (City, State, and ZIP Code) Department of Chemistry Baker Laboratory, Cornell University Ithaca, New York 14853	7b. ADDRESS (City, State, and ZIP Code) Chemistry Division 800 N. Quincy St. Arlington, VA 22217
8a. NAME OF FUNDING / SPONSORING ORGANIZATION Office of Naval Research 8b. OFFICE SYMBOL (If applicable)	9. PROCUREMENT INSTRUMENT IDENTIFICATION NUMBER N00014-84-K-0656/P00002
8c. ADDRESS (City, State, and ZIP Code) Chemistry Division 800 N. Quincy St. Arlington, VA 22217	10. SOURCE OF FUNDING NUMBERS PROGRAM ELEMENT NO. / PROJECT NO. / TASK NO. / WORK UNIT ACCESSION NO

11. TITLE (Include Security Classification)
Probing Interfacial Structure and Composition with X-ray Standing Waves

12. PERSONAL AUTHOR(S)
Hector D. Abruna and Michael J. Bedzyk

13a. TYPE OF REPORT	13b. TIME COVERED	14. DATE OF REPORT (Year, Month, Day)	15. PAGE COUNT
Technical	FROM _____ TO _____	90/6/4	2

16. SUPPLEMENTARY NOTATION

17 COSATI CODES			18. SUBJECT TERMS (Continue on reverse if necessary and identify by block number)
FIELD	GROUP	SUB-GROUP	X-rays, synchrotron radiation, standing waves, interfaces

19. ABSTRACT (Continue on reverse if necessary and identify by block number)

We present a brief description of the principles of x-ray standing waves based on Bragg diffraction and total external reflection. The broad range applicability of this technique to probe interfacial structure and composition is illustrated by considering representative examples from the areas of adsorbate structures in ultra-high vacuum, potential dependent changes in an electrochemical systems and the study of ionic distributions at a model membrane.

Keywords:

is given for

20. DISTRIBUTION / AVAILABILITY OF ABSTRACT	21. ABSTRACT SECURITY CLASSIFICATION
☒ UNCLASSIFIED/UNLIMITED ☐ SAME AS RPT ☐ OTIC USERS	unclassified
22a. NAME OF RESPONSIBLE INDIVIDUAL H. D. Abruna	22b. TELEPHONE (Include Area Code) (607) 255-4720 / 22c. OFFICE SYMBOL

DD FORM 1473, 84 MAR — 83 APR edition may be used until exhausted. All other editions are obsolete.

SECURITY CLASSIFICATION OF THIS PAGE
Unclassified

Probing Interfacial Structure and Composition with X-Ray Standing Waves

Héctor D. Abruña* and Michael J. Bedzyk#
*Department of Chemistry, Baker Laboratory
#Cornell High Energy Synchrotron Source
and School of Applied & Eng. Physics
Cornell University
Ithaca, New York 14853

Abstract:

We present a brief description of the principles of x-ray standing waves based on Bragg diffraction and total external reflection. The broad range applicability of this technique to probe interfacial structure and composition is illustrated by considering representative examples from the areas of adsorbate structures in ultra-high vacuum, potential dependent changes in an electrochemical systems and the study of ionic distributions at a model membrane.

1. Introduction:

The reactivity of an interface is extensively determined by its composition and structure [1]. Thus, structural, compositional and distributional studies, at interfaces can yield very valuable information not only from a fundamental scientific point of view but also from technological and economic perspectives. Of particular importance are interfacial structural changes that may arise as a result of various physicochemical perturbations such as applied potential, pH, and others since in many cases these changes will greatly influence reactivity. These investigations are relevant to the understanding of structural, distributional and compositional effects on many fundamental problems such as electron transfer, adsorption, catalysis, corrosion, and the distribution of ionic species at charged surfaces especially at solid/liquid interfaces. However, experimental studies involving these interfaces are confronted by various difficulties; the principal one being the inability of many structural techniques to probe a condensed phase. As a result, there is a lack of information at the molecular and atomic levels concerning these interfaces.

Because of their penetrative power through condensed phases x-rays are ideally suited for in-situ studies of interfaces in general and solid/liquid interfaces in particular. The recent advent of powerful x-ray synchrotron sources, has made experiments of this type feasible. Synchrotron sources offer a broad spectral range of polarized, highly collimated x-rays with intensities that are 10^3 to 10^6 higher than those of a conventional x-ray tube [2]. The high intensity, natural collimation, polarization, and tunability over a broad energy continuum make x-rays from synchrotron sources an extremely sensitive structural probe of interfacial and surface structure. Surface sensitive x-ray techniques include: X-ray Standing Waves (XSW) [3], Grazing Incidence X-ray Diffraction (GIXD) [4], techniques based on the theory of Crystal Truncation Rods (CTR) [5], and Surface Extended X-ray Absorption Fine Structure (SEXAFS) [6].

Here we concentrate on a description of the XSW technique and its application to structural studies, at the atomic and molecular levels of interfaces in general, with emphasis on solid/liquid interfaces.

2. Theoretical Description:

When two coherently related travelling plane waves having the same wavelength pass through each other (Figure 1) their superposition results in a standing wave of period $D = \lambda/2 \sin\theta$; where λ is the wavelength of the travelling waves, and 2θ is the relative angle between them. Such interference effects are present in numerous situations such as water waves in a ripple tank, sound waves confined to a closed pipe and others. The generation of standing waves is not limited to mechanical waves but can also be present in electromagnetic waves such as x-rays.

To generate an XSW one can employ either a reflection or a transmission geometry. In the transmission geometry, the two travelling plane waves can be prepared by use of a Laue interferometer as has been demonstrated by Materlik et. al. [7].

In this account, we will focus on the reflection geometry which is not only more versatile, but in addition, experimentally less demanding.

In the reflection geometry the incident and reflected plane waves interfere to generate an XSW as depicted in Figure 2 A. Since generation of a standing wave requires both an incident and a reflected wave, we need to identify the conditions that will fulfill this requirement. In the x-ray regime this can be achieved by Bragg diffraction or total external reflection (Figure 2B).

Conventional XSW are generated using dynamical Bragg reflection [8] from perfect single crystals (typically Si, Ge, GaAs)[9-11] although metallic single crystals have also been employed [12]. The periodicity of the standing wave field is equivalent to the d-spacing of the (hkl) diffracting planes. Since the standing wave periodicity is determined by the d-spacing of the generating substrate this technique is a precise tool

(± 1% of the d-spacing)[9] for measuring bond-lengths between adsorbate atoms and surface/bulk lattice positions over the range of 1 to 4Å (i.e. typical d-spacings for single crystals). In Bragg diffraction XSW measurements, distances are extracted modulo-d (that is relative to the diffraction planes) so that it is inappropriate to employ this method for structural determinations of systems extending over several tens of angstroms such as ionic distributions at charged interfaces. In this case, XSW having a longer period would be much more appropriate. Such long period XSW can be generated by Bragg diffraction from layered synthetic microstructures (LSM)(vide-infra) which have d-spacings ranging from 20 to 200 Å [13,14] or by employing total external reflection from a mirror surface (vide infra)[15]. The longer periods are due to the fact that at a given wavelength the reflection occurs at smaller angles (θ) than in the case of Bragg diffraction from single crystals. We will discuss these various techniques and present examples on their applicability.

Figure 2A depicts the formation of a standing wave field by the interference between incident and reflected plane waves with wavevectors k_O and k_R, respectively. The standing wave electric field intensity is given by:

$$I(\theta,z) = |\bar{\varepsilon}_o + \bar{\varepsilon}_R|^2 = |E_O|^2\ [1+R+2\sqrt{R}\cos(\nu-2\pi Q_z)], \qquad (1)$$

where:

$$\bar{\varepsilon}_o(r,t) = E_o\ \exp\{i[\omega t - 2\pi(k_x x - k_z z)]\}$$
$$\bar{\varepsilon}_R(r,t) = E_R\ \exp\{i[\omega t - 2\pi(k_x x + k_z z)]\} \qquad (2)$$

are the incident and reflected plane waves if their respective wavevectors k_O and k_R, lie in the x-z plane with the z-axis normal to the surface. $Q = k_O - k_R$ is the momentum transfer with a magnitude given by:

$$|Q| = Q = 2 \sin\theta/\lambda = 1/D, \qquad (3)$$

where D is the period of the SW. The variables $R(\theta)$ and $\nu(\theta)$ in equation 1 correspond, respectively, to the intensity and the phase of the reflected wave relative to the incident wave.

The above description is generally applicable to XSW generated in reflection geometry. We consider below the specific cases of Bragg reflection and total external reflection.

A. X-ray Standing Waves based on Bragg Reflection:

For the case of XSW based on Bragg reflection, the standing wave can extend well beyond the reflecting surface and estimates of this coherence length range to values as large as 1000Å [14a]. The nodal and antinodal planes of the standing wave are parallel to the diffracting planes (Figure 3B) and for Bragg reflection, the nodal wavelength corresponds to the d-spacing of the diffracting planes. As the angle of incidence is advanced across the strong Bragg reflection, the relative phase between the incident and reflected plane waves (at a fixed point in the crystal) changes by π (Figure 3A). Due to this phase change, the antinodal planes of the standing wave field move in the -H direction normal to the diffraction planes by 1/2 of a d-spacing, from a position halfway between the (h,k,l) diffracting planes (low angle side of the Bragg reflection) to a position that coincides with them (high angle side of the Bragg reflection). (Figure 2B) Thus, the standing wave can be made to sample an adsorbate or overlayer at varying positions above the substrate interface.

For an atomic overlayer which is positioned parallel to the diffracting planes, the nodal and antinodal planes of the standing wave will pass through the atom plane as the angle is advanced. Using an incident x-ray beam energy at or beyond the absorption edge of the atoms in the overlayer, the fluorescence emission yield will be modulated in a characteristic fashion as the substrate is rocked in angle. The yield can be expressed as an integral that incorporates a distribution function f(z) for the atoms in the adlayer:

$$Y(z,\theta) = \int I(z,\theta)\, f(z)\, dz \qquad (4)$$

Figure 4 depicts the angular dependence of the electric field intensity (or fluorescence yield) for an adsorbate layer located at varying positions with respect to the diffracting planes. The phase and amplitude of this modulation (or so-called coherent position and coherent fraction) are a measure of the mean position <z> and width $\sqrt{<z>^2}$, respectively of the distribution F(z) of atoms in the overlayer. The coherent fraction (f_c) and coherent position (ϕ_c; which is equal to (<z>/d)) are defined as the amplitude and phase, respectively, of the m^{th} Fourier component for the distribution of atoms in the adlayer, and are incorporated into the yield equation as:

$$Y(z,\theta) \propto [(1+R+2\sqrt{R}\, f_c \cos(v-2\pi\, \phi_c)] \qquad (5)$$

For example if all the atoms were at the same z position (i.e. a distribution described by a delta function) the coherent fraction would be unity. Conversely, if the atoms were randomly distributed the coherent fraction would be zero. For intermediate cases the coherent fraction would vary from zero to one. For the case of a Gaussian distribution, the coherent fraction would be given by; $f_c = \exp\{-2\pi^2\sigma^2/d^2\}$ which is of the same form as the Debye-Waller expression.

Since the z scale of the Bragg diffraction XSW is mod-d, if several coherent positions (in z) are possible for the adsorbate, a single measurement will not be sufficient to unambiguously determine these positions. Thus, XSW measurements with a different period, and thus different Fourier components, (such as higher order Bragg diffraction measurements or total external reflection measurements) must be performed to allow such an assignment.

Although the characteristic modulo-d length scale of a few angstroms of single crystals is ideal for determining bond lengths between atom layers at single crystal surfaces, it is inappropriate for the structural determination of systems extending over several tens of angstroms (e.g. ionic distributions at charged surfaces).

An alternative to single crystals is the use of synthetic layered microstructures (LSM)[14]. For Bragg diffraction purposes, LSMs are depth-periodic structures consisting of alternating layers of high and low electron density materials (such as tungsten and silicon, or platinum and carbon), and are of high enough quality to produce strong Bragg diffraction. LSMs provide several advantages, over natural crystals, for x-ray standing wave experiments:

(1) LSMs can be produced with fundamental d-spacings ranging from 20 to 200Å, as compared to a few angstroms for natural crystals. These large d-spacings give rise to long period standing waves which are optimally suited to investigate systems with a longer length.

(2) The experimenter can choose to synthesize LSMs from a wide range of materials; whereas there is only a limited choice of natural crystals. Even more important, the experimenter can choose the material to be used as the multilayer's top surface.

(3) Experimental reflection curves from LSMs compare well with predictions from dynamical diffraction theory, and peak reflectivities are as high as 80%. Therefore, a well defined standing wave can be produced.

(4) Due to the relatively small number of layer pairs which effect Bragg diffraction, LSMs have a rather large energy bandpass, and Bragg reflection angular widths of the order of milliradians rather than microradians, as in natural crystals. This last point is important as it considerably simplifies experimental design.

(5) In addition to being good diffracting structures, LSMs possess surfaces of mirror quality, making them excellent x-ray reflectors as well. Therefore, they can also be used as substrates for generating total external or specular reflection XSWs which we describe below.

B.Total External Reflection X-Ray Standing Waves (TER-XSW):

Since the refractive index of matter for x-rays is less than unity [16], when x-rays are incident on a mirror surface at an angle smaller than the critical angle, the refracted wave cannot penetrate through the reflecting surface. This means that all the incident wave energy is going into the reflected wave and total external reflection is taking place (Fig. 2B). Under this condition only an exponentially damped evanescent wave penetrates into the medium below the reflecting surface. At the same time, the incident and specularly reflected plane waves interfere to form a standing wave in the more optically dense medium above the mirror surface. The angular dependence of the reflectivity and phase of the reflected plane wave are depicted in Figure 5a. Analogous to XSW generation via Bragg diffraction, there is a change in the relative phase (by π) between the incident and reflected waves. Regarding the phase at $\theta = 0$, the reflected plane wave is completely out of phase with respect to the incident plane wave at the mirror surface. Thus, at $\theta=0$ a node is at the mirror surface and the first antinode is at infinity since $D= \infty$ (Figure 5b). As the angle of incidence is increased, the first antinode moves inward, in a direction normal to the surface, until at the critical angle it coincides with the mirror surface. The trailing antinodes (Figure 5b) follow behind with a periodic spacing given by:

$$D = \lambda / (2\sin\theta) \qquad (6)$$

In this context one can also define a critical period D_c which is that when $\theta = \theta_c$ where θ_c is the critical angle. It should be mentioned that for 1Å wavelength x-rays values of θ_c range typically from 1-8mrad so that the critical period ranges from 80 to 500Å.

3. Experimental aspects:

X-ray standing wave measurements are, in general, experimentally very demanding. Although the experimental set-up is not particularly complex, alignment of

the sample relative to the beam is critical. An XSW experiment typically consists of monitoring some signal proportional to the standing wave electric field intensity as the angle of incidence is scanned through the total external reflection or across a Bragg reflection. A typical experimental set up is shown in Figure 5 and consists of i) a collimated beam whose intensity I_0 is monitored with an ion chamber, ii) a sample stage, iii) a reflected beam monitor I_R and iv) a fluorescence detector at 90° relative to the x-ray beam. Of particular importance in this experiment is the angular precision of the sample stage since a typical reflection width for a single crystal will be of the order of tens of microradians and a few milliradians for LSMs.

At each angular position, a complete x-ray fluorescence spectrum is collected and later analyzed so as to accurately remove background and other undesirable contributions to the signal.

4. Analysis of data and interpretation of results:

Analysis of x-ray standing wave data is based on a fit of the data (reflectivity and fluorescence yield) to those predicted from theory. However, the data must first be treated to extract yields corrected for background and other contributions. In general, the fluorescence yield is recorded as a function of angle of incidence. An energy dispersed spectrum for each angle is recorded in digital memory. Fitting of the desired characteristic emission line to an assumed functional form (usually a combination of Gaussian functions) and subtraction of an extrapolated polynomial background serve to render the data in a form suitable for reconstruction of the fluorescence yield as a function of the angle of the incident radiation.

The electric field intensity at a given point above the reflecting surface must either be calculated from dynamical diffraction theory [8] or from an optical theory approach. The latter approach is generally based on a formalism in which the medium is divided into parallel slabs [17]. The continuity of the tangential components of the

electric and magnetic fields at each of the resulting interfaces is the essential requirement invoked to obtain a recursion relation (containing Fresnel coefficients) describing the E-field amplitudes at each interface of the incident, reflected and refracted waves. Such a treatment is applicable to the total external reflection condition as well as to Bragg diffraction.

The layered medium approach is particularly well suited for analysis of standing waves in multilayered structures [14,18]. The recursion relation employed generally has the following form:

$$R_{j,j+1} = a_j^2 \left[\frac{R_{j+1,j+2} + F_{j,j+1}}{1+R_{j+1,j+2}\,F_{j,j+1}}\right] = \frac{E_j^R(o)}{E_j(o)} \qquad (7)$$

where $R_{j,j+1}$ = ratio of reflected E-field amplitude to incident E-field amplitude for j^{th} layer

$R_{j+1,j+2}$ = ratio of reflected wave amplitude to incident wave amplitude for $j+1^{th}$ layer

$F_{j,j+1}$ = Fresnel coefficient for j^{th} layer

a_j = complex amplitude factor at the j, j+1 interface.

The reflectivity at a given interface is the squared modulus of $R_{j,j+1}$. The total reflectivity at a given angle of a structure consisting of n layers is obtained by applying the recursion relation n-1 times from the substrate (or from the extinction length) to the topmost layer.

The description in the total external reflection region becomes more complicated since absorption and refraction effects in the region above the reflecting surface can no longer be ignored as is typically done for Bragg diffraction from single crystals.

5. Applications:

In this section we present results, in some detail, from various experiments which exemplify the applicability of XSW measurements. These include measurements with single crystals, LSMs and mirror surfaces.

A. X-Ray Standing Wave Study of Iodine on Ge(111):

Conventional XSW measurements, which employ dynamical Bragg diffraction from perfect single crystals to generate an x-ray standing wave inside the crystal and above the crystal surface, are well suited for determining bond-length distances in adsorbate structures since the period of this SW is determined by the diffraction plane spacing which is typically of the order of a few ångstroms. Since the SW is generated from deep inside the crystal, the resulting structural information links the position of surface atom layers to the to the bulk structure. Thus XSW measurements of this type are complimentary to other surface structure sensitive techniques, such as low-energy electron diffraction (LEED), which gives in-plane crystallographic information about the surface layer, or SEXAFS, which gives the local geometry of a surface atom layer in terms of nearest neighbor distances.

In a recent ultra high vacuum (UHV) study [19] of a monolayer (ML) of iodine adsorbed onto an atomically clean (2x8) reconstructed surface of Ge(111), we were able to show that the iodine saturates the Ge surface dangling bonds and causes the Ge surface atoms to take up bulk-like positions. A side view of this surface structure is depicted in Fig. 7. In this analysis the XSW measurement was used to determine Δd_I, the position of the iodine atom layer relative to the (111) Ge bulk-lattice planes. This information was then combined with a previous SEXAFS determination of d_{GeI}, (the I-Ge bond length for this same surface system) [20] to determine the position of the surface Ge(111) surface atom layers relative to the bulk lattice (i.e. Δd_{GeI}).

The surface was prepared in UHV by Ar^+ sputtering and annealing to 650°C until a (2x8) LEED pattern was observed. An electrolytic iodine source was then used to deposit 1.5 ML of I onto the clean Ge(111) surface at room temperature. This "as deposited" surface was then annealed to 400°C for 5 min. At this point the iodine coverage was consistently 1 ML and the LEED pattern was a clear (1x1).

The XSW measurements of the "as deposited" and annealed I/Ge(111) surfaces are shown in Fig. 8. For these XSW measurements, the I_{L_3} photoelectron yield was monitored with a cylidrical-mirror analyzer while scanning across the Ge(111) Bragg reflection with a 6.0 keV energy incident x-ray beam. Although the phase of the I modulation for the two scans is essentially the same, it is clear that the modulation amplitude of the "as deposited" I yield is weaker than for the annealed case. Upon analyzing the data according to equation 5, the "as deposited" surface has an iodine coherent position of ϕ_C = 0.85±.01 and a coherent fraction of f_C=0.65±.01. For the annealed surface the vales were ϕ_C=0.87±.01 and f_C=0.97±.02

The coherent coverage, $\Theta_C=f_C\Theta$, where Θ is the total coverage, is 1 ML before and after the anneal. This constancy of the coherent coverage combined with the constancy of the coherent position indicates that the annealling process primarily causes the desorption of half a monolayer of randomly distributed iodine.

B. Potential Dependence of Packing Density and Distributional Changes of Iodine at a Pt/C LSM:

The adsorption of iodide at single crystal and polycrystalline platinum electrodes has been the subject of numerous studies using low energy electron diffraction (LEED), Auger electron spectroscopy (AES), [21] voltammetric techniques, [22] and x-ray absorption spectroscopy (XAS)[23]. Immersion of a Pt(111) surface into aqueous iodide (or HI) solutions results in the formation of an ordered ad-layer of iodine atoms [21]. In addition, the Pt(111)/I system possesses a rich potential-dependent coverage

isotherm, which has been characterized in and ex-situ by XAS [23] and AES [24], respectively. The various features of this isotherm are interpreted in terms of potential dependent structural and distributional changes. The purpose of this work was to employ the XSW technique for an in-situ study of the potential dependence of the Pt/I system, using the previously mentioned body of data as a guide.

In this study we employed a Pt/C LSM (40.8Å d-spacing) as an electrode in contact with a pH 6.7 solution containing 0.1M Na_2SO_4 and 10μM NaI. We operated in the thin layer configuration where the electrode was in contact with a thin layer (typically about 5μm) of electrolyte.

The first thing to keep in mind in this study is the inadequacy of coherent position and coherent fraction in describing the nature of the distribution of species in the vicinity of an electrode surface. These quantities are relevant only when describing symmetrical atomic distributions centered around a given mean (<z>) position. For an extended unsymmetrical distribution, a model for N(z) must be chosen and the standing wave electric-field intensity I(θ,z) must be averaged over the entire distribution:

$$Y(\theta) = \int I(\theta,z)N(z) \qquad (8)$$

In this study, we chose a model (Figure 9A) that has three basic components: (1) an ad-layer (step) of specifically adsorbed (i.e. in contact with the electrode surface) iodine atoms, (2) an exponential tail of iodide extending out into solution with a characteristic decay length k, (the diffuse layer), and (3) a second layer (step) of width equal to the thickness of the solution layer, depicting bulk iodide. This model can be expressed as:

$$N(z) = \begin{cases} N_{ad} & 0 \le z \le t_{ad} \\ N_{diff} \exp(-z/k) + N_{bulk} & t_{ad} < z \le t_{sol} \end{cases} \qquad (9)$$

where: N_{ad} is the concentration of specifically adsorbed iodine atoms, t_{ad} is the thickness of the ad-layer, N_{diff} is the initial concentration of iodide in the diffuse layer, k is the decay length of this diffuse layer, N_{bulk} is the iodide bulk concentration, and t_{sol} is the

thickness of the solution layer. An exponential decay was used to model the diffuse layer because it is frequently employed in simple theoretical descriptions of the electrical double layer [25]. The yield can now be calculated using the distribution N(z) defined above (Equation 9) in the integral (Equation 8). N_{diff} and N_{bulk} were expressed as fractional values of N_{ad} and the distribution was normalized using the condition:

$$Y_{OB} = \int N(z)dz, \qquad (10)$$

where Y_{OB} is the measured off-Bragg fluorescence yield which is proportional to the total number of I/I^- species present in the solution layer t_{sol}. Thus, the model has three free parameters: the ad-layer thickness t_{ad}, the fractional quantity N_{diff}/N_{ad}, and the decay length k. The remaining parameters are either known or experimentally determined.

From theoretical calculations we find that the yield is very sensitive to distributional changes as expressed by the model. Figures 9B-D illustrate the effects of varying t_{ad}, the ratio N_{diff}/N_{ad}, and k, on the XSW fluorescence yield. In these calculations, x-rays with incident energy of 6.0keV reflect from the surface of a Pt/C LSM (d=40.8 Å) in contact with a solution layer 5.24μm thick, containing a 10μM bulk concentration of iodide, and encapsulated by a 6μm polypropylene film.

When the model (Equation 9) is simplified to consist of only an adlayer:

$$N(z) = N_{ad} \qquad 0 \le z \le t_{ad}, \qquad (11)$$

the standing wave yield can be expressed as (using Equations (8) and (10)):

$$Y(\theta) = T\{1+R+2\sqrt{R}[\sin(\pi Q t_{ad})/(\pi Q t_{ad})]\cos(v-2\pi Q z_0)\}, \qquad (12)$$

where: z_0 is the position of the step's center, T represents the electric-field magnitude of the incident wave at z_0, and R and v correspond to the intensity and phase of the Bragg reflected wave relative to the incident wave at z_0. Equation 12 describes the yield from an adsorbed layer centered at $z=z_0$ with a z-projected concentration N_{ad} large enough to neglect contributions to the total XSW yield from the bulk. For very small values of t_{ad}, $\sin(\pi Q t_{ad})/(\pi Q t_{ad})$ reduces to 1, and the full interference term is included in the yield

evaluation. It is for this condition that we expect to observe the largest amplitudes and phase modulations in the XSW signal (Figure 9B, solid curve). When $t_{ad}=d=1/Q$, $\sin(\pi Qt_{ad})/(\pi Qt_{ad})$ is zero and the yield is given by T{1+R}. This is the same XSW yield expected from a totally random distribution of atoms. Here the phase information is lost and the amplitude of the signal is only dependent on the substrate's Bragg reflectivity (Figure 9B, dashed curve). For values of t_{ad} between these limiting cases, $\sin(\pi Qt_{ad})/(\pi Qt_{ad})$ varies smoothly between 1 and 0.

The effect of including the diffuse layer along with the adsorbed layer in the model (Equation 9), corresponds to a superposition of a random-like component to the coherent XSW yield from the ad-layer (provided that the thickness t_{ad} is narrow with respect to the substrate's d-spacing), in a ratio proportional to the population in each layer. In here, the number of atoms in the diffuse layer is controlled by the decay length k and the initial concentration N_{diff} (Figure 9 C,D). What is important to note, is the sensitivity of the XSW technique to these distributional changes. Adding a diffuse layer with a fall-off length of only 10 Å produces a dramatic change in both the amplitude and the phase of the calculated signal (Figure 9D). Furthermore, appreciable differences are seen when the diffuse layer population is changed by varying N_{diff} (Figure 9C). Thus, in principle, the XSW method is extremely sensitive to subtle changes in atomic/ionic distributions at the electrode/electrolyte interface.

The angular dependence of the I_L fluorescence yield for each of the potentials studied, is shown in Figure 10. As we discussed previously, changes in the phase and amplitude of the standing wave signal are indicative of distributional changes in the direction normal to the substrate surface. (Table I)

It can be seen that the peak in each fluorescence yield curve does not occur at the same angular position (Figure 10), but shifts smoothly from a position on the high side of the Bragg angle (θ_B) for -0.1V, to a position approximately equivalent to θ_B at applied potentials of +0.3V and +0.4V, and finally back to an angle greater than θ_B at

+0.49V. In addition, the amplitude of the modulation in each of the fluorescence yield profiles changes with potential.

We also observe different values of the off-Bragg fluorescence yield at different applied potentials. These differences correspond to changes in the total amount of I^-/I species sampled by the incident and reflected beams.

The background slope, the relative off-Bragg yield on the low and high angle sides of the Bragg reflection, also shows a marked potential dependence (Table I). At the more negative potentials (-0.9V and -0.45V) this slope is negative, and its magnitude is characteristic of a random distribution of species in the solution layer. In this case, the off-Bragg fluorescence yield is proportional only to the illuminated volume of solution, which in turn varies as $1/\sin\theta$. Most notably, for an applied potential of -0.1V the background slope becomes positive. For all of the remaining potentials (+0.15V to +0.49V) there is a negative slope of varying magnitude, but which never approach the value expected for the random case.

All of the trends observed above can be understood in terms of changes in the distribution of iodine/iodide species at the electrode/electrolyte interface as described by the model mentioned above.

To quantify the results presented above, we have χ^2 fitted the data to theoretical yields based on the model defined in Equation 9. The results are presented in Table II.

It can be ascertained that the decay length varies smoothly from -0.1V to +0.4V, followed by an abrupt decrease at the highest potential investigated. In contrast, we note exactly the opposite behavior for the fractional concentration. What is most remarkable is the magnitude of the variations in these parameters with potential, especially in light of the fact that iodide is present in solution in a ratio of 1 to 10,000 relative to the sulfate dianion in the supporting electrolyte. Thus, we are able to observe tremendous distributional rearrangements of a very small amount of iodide, over considerable length scales, with Ångstrom resolution.

It should be noted that the observed changes in the decay lengths of the diffuse layer are opposite to those expected from electrostatic arguments, from which we would anticipate a decrease in the decay length as the surface charge becomes more positive. However, we would also expect that the very large excess of the dianion in the supporting electrolyte, in addition to being largely responsible for charge screening effects, will respond much more rapidly to surface charge changes than the iodide ion. Furthermore, primitive double layer models that neglect interion interactions are invalidated by the high ionic strength of our system.

The changes in ad-layer normalized coverage with applied potential are also listed in Table II. These values were obtained by taking the off-Bragg yield at each potential and subtracting the contribution due to the diffuse layer, as determined from the fitting parameters κ and N_{diff}/N_{ad}.

The variations in the normalized coverage are analogous to packing densities observed on Pt(111) from dilute NaI solution by in-situ x-ray absorption spectroscopy [23] and on emersed Pt(111) by Auger electron spectroscopy [24]. In these cases, these changes are attributed to structural changes in the adsorbed iodine ad-layer.

Since the changes observed in the normalized coverage in this experiment are in excellent agreement with the changes in the packing density measured on a Pt(111) electrode surface we believe that a similar structural transition takes place for the iodine ad-layer formed at the Pt surface of the Pt/C LSM employed in this work.

Based on an analysis of the standing wave and off-Bragg yield measurements, we note a marked accumulation of iodide in the diffuse layer, weakly associated with the adsorbed iodine, when the Pt surface is not saturated by iodine adatoms (-0.1V). This striking association of iodide with the iodine ad-lattice is perhaps driven by the hydrophilic character of the unsaturated Pt surface. In addition, the increase in the adsorbed iodine packing density to saturation coverage is accompanied by an abrupt decrease in the concentration of this accumulated iodide. Thus, the potential dependent

structural transformation in the iodine ad-lattice might be viewed as a phase transition, in which iodide anions in the liquid-like arrangement of the diffuse layer are incorporated into the crystalline-like structure of the iodine ad-lattice. This results in a saturated, possibly hydrophobic Pt surface and in the concomitant decrease in the concentration of iodide in the diffuse layer associated with the adsorbed iodine.

In this work, we were able to follow, in-situ, potential dependent distributional changes of an ionic component, with Ångstroms resolution in the direction normal to the electrode surface. Although the model chosen to describe this distribution was primitive it was consistent with all experimental observations. The use of more complex models, using liquid-pair distribution functions, might allow for a more rigorous description of the diffuse layer and its changes. However, in order to unambiguously determine the value of each of the parameters used to define these types of distributions, standing wave measurements over higher order Bragg reflections as well as the total external reflection regime, need to be carried out. However, the applicability and power of the XSW technique to these studies is clear.

C. X-ray Standing Wave Measurements based on Mirror Reflection:

As illustrated in Fig. 2b, the total external reflection condition occurs between $\theta=0$ and $\theta = \theta_c$ (where θ_c is a few milliradians). Over this angular range the period of the generated XSW varies between infinity and several nanometers in length. This characteristically long and variable period distinguishes the total external reflection XSW from the Bragg diffraction XSW. The similarity between the two cases is that a π radian XSW phase shift occurs in both cases as the incident angle is advanced through the total reflection condition.

Since the fluorescence yield is proportional to the E-field intensity at the center of an atom, we can observe the angular dependence of the XSW, as shown in Fig. 5b, by monitoring the fluorescence signal from a marker layer of atoms that is a mean distance

<z> above the mirror surface. Observing the π radian phase shift can most easily be done by placing the marker layer at the surface. This is the evanescent-wave condition [26], which has the surface E-field intensity going from a node to an antinode as θ increases from 0 to θ_c. This effect, which is described by the z=0 curve in Fig. 5b, is routinely used for enhancing surface fluorescence and surface diffraction.

To clearly observe the compression of the XSW as θ increases, the following experimental conditions should exist: (1) the marker layer should be at a mean position <z> so that the distance of the layer to the surface is greater than the critical period Dc, (2) the width of the marker layer ($\sqrt{\langle z^2 \rangle}$) should be much smaller than <z>, and (3) the refractive effects of the overlayer that contain the marker layer should be much weaker than the refractive effects of the mirror (i.e. the density of the overlayer should be much smaller than that of the mirror). If the above conditions are satisfied, then there will be $\frac{\langle z \rangle}{D_c} + \frac{1}{2}$ modulations in the fluorescence yield of the marker between $\theta = 0$ and $\theta = \theta_c$. This is exemplified by the 2.5 modulations that occur over the 0 to θ_c interval in Fig. 5b for the $z=2D_c$ curve.

Such a modulated fluorescence yield was recently reported for a Zn atom layer embedded in the top arachidate bilayer of a Langmuir-Blodgett (LB) multilayer film which was deposited on the surface of a gold mirror [15a]. As shown in Figure 11, three full oscillations in the Zn fluorescence yield occur before reaching the critical angle of gold, indicating that the Zn layer is at $\langle z \rangle = 2.5D_c = 200$ Å (The critical angle for gold at the incident energy of 9.8keV is about 7.8 mrad (Figure 11a) so that the critical period D_c is about 80Å (Equation 6). The value of <z> was more precisely determined to be 218 Å from a χ^2 fit of the data to theoretical yields based on a layered model. From this fit, we also determined that the 2σ thickness of the Zn layer was 24 Å . Upon heating, this LB multilayer went through an irreversible melting transition at T = 100°C, resulting

in an inward spread of the Zn layer. The χ^2 fit to the data in Figure 11c for T = 105°C indicates a Zn mean position of <z> = 170 Å and a 2σ width of 110 Å. A similar transition was observed in an earlier XSW study where Bragg diffraction from an LSM was used to determine the Zn distribution in a LB arachidate trilayer [14d].

Since the standing wave samples the selected atom distribution with a variable period D, we are in effect measuring the Fourier transform of that distribution over a continuous range in Q = 1/D (i.e. a scan in Fourier space). With a variable period ranging from 10's of angstroms to 100's of angstroms, this x-ray standing wave technique is ideally suited to measure surface and interface layered structures which have natural length scales in the 10 to 1000 Å regime such as the one described above.

Another type of structure amenable to investigation with this long period XSW probe is the diffuse-double layer at a charged solid/liquid interface. We have recently made a direct measurement of the ionic distribution profile in an electrolyte in contact with a charged phospholipid membrane [15b]. The 30 Å thick membrane was supported on a silicon/tungsten LSM. The x-ray standing waves were generated by total external reflection from the surface of the Si/W LSM and by Bragg diffraction from the 35 Å periodic structure of the LSM. The top of the membrane formed a negatively charged sheet of phosphate ions in contact with a 0.1mM aqueous $ZnCl_2$ solution. The coverage of the condensed Zn layer (which partially neutralized the phosphate layer) and the Debye length of the electrostatically attracted diffuse Zn ion layer were measured with x-ray standing waves at three different pH values and the results (Table III) were consistent with the Gouy-Chapman-Stern model [25].

6. Conclusions and Future Directions:

The use of x-ray standing waves is yielding valuable insights on interfacial structure and composition. Future applications of this novel technique to the study of interfaces will yield extremely important and fundamental information that will affect not only our

understanding and control of interfacial reactivity, but the field of surface chemistry as a whole.

Acknowledgements:

This work was generously supported by the Materials Chemistry Initiative of the National Science Foundation, the Office of Naval Research, the Materials Science Center at Cornell University, the Army Research Office, Eastman Kodak Co., Dow Chemical Co. and Xerox Corp. HDA is a recipient of a Presidential Young Investigator Award and a Sloan Foundation Fellowship.

The help of G. M. Bommarito, J.H. White, D. Acevedo, L. E. Berman, Q. Shen, G. Navrotski M. McMillan, and the CHESS staff is greatly appreciated. The work described here was performed at the Cornell High Energy Synchrotron Source (CHESS) which is supported by the Division of Materials Research of the National Science Foundation.

Literature Cited:

1 a. Adamson, A. W. Physical Chemistry of Surfaces, Wiley, New York 1982

b. Somorjai, G. A.; Chemistry in Two Dimensions: Surfaces, Cornell University Press, Ithaca, 1981

c. Israelachvili, J. N.; Intermolecular an Surface Forces, Academic Press, London, 1985

2 Winick, H.; Doniach, S. eds.; "Synchrotron Radiation Research," Plenum, New York, 1980.

3 Batterman, B.W.; Phys. Rev.,1964, 133, A759

4 a. Marra, W.C.; Eisenberger, P.; Cho, A.Y.; J. Appl. Phys.,1979, 50, 6927

b. Eisenberger, P.; Marra, W.C.; Phys. Rev. Lett.,1981, 46, 1081

c. Marra, W.C.; Fuoss, P.H.; Eisenberger, P.E.; Phys. Rev. Lett.,1982, 49, 1169

5 Robinson, I.K.; Phys. Rev. B,1986, 33, 3830

6 a. Citrin, P.H.; Journal de Physique Colloque, 1986, C8, 47, 437

b. Lee, P.A.; Citrin, P.H.; Eisenberger, P.; Kincaid, B.M.; Rev. Mod. Phys.,1981, 53, 769

c. Teo, B.K.; "EXAFS: Basic Principles and Data Analysis," Springer Verlag, Berlin, 1986.

7 Materlik, G.; Frahm, A.; Bedzyk, M. J.; Phys. Rev. Lett. 1984, 52, 441

8 M.von Laue, *Roentgenstrahlinterenzen* (Akademische Verlargsgesellshaft, Frankfurt, 1960). For a review, see B. W. Batterman and H. Cole, Rev. Mod. Phys. 36, 681 (1964).

9 Bedzyk, M.J.; Materlik, G.; Phys. Rev. B,1985, 31, 4110

10 Cowan, P.L.; Golovchenko, J.A.; Robbins, M.F.; Phys. Rev. Lett.,1980 44, 1680

11 J. Zegenhagen, J; Huang, K.-G.; Gibson, W.M.; Hunt, B. D.; Schowalter, L.J. Phys. Rev. B, 1989, 39, 10254.

12 a. Woodruff, D.P.; Seymour, D.L.; McConville, C.F.; Riley, C.E.; Crapper, M.D.; Prince, N.P.; Jones, R.G.; Phys. Rev. Lett.,1984, 58, 1480.

b. Woodruff, D.P.; Seymour, D.L.; McConville, C.F.; Riley, C.E.; Crapper, M.D.; Prince, N.P.; Jones, R.G.; Surface Science, 1988, 195, 237.

c. Materlik, G.; Zegenhagen, J.; Uelhoff, W.; Phys. Rev. B, 32, 5502 (1985).

d. Materlik, G.; Schmah, M.; Zegenhagen, J.; Uelhoff, W.; Ber. Bunsenges. Phys. Chem., 91, 292 (1987).

13 Underwood, J.H.; Barbee, T.W.; in AIP Conf. Proc., 75, 170, D.T. Atwood, B.L. Henke, eds., AIP, New York, 1981.

14 a. Barbee, T.W.; Underwood, J.H.; Optics Comm.,1983, 48, 161

b. Barbee, T. W.; Warburton, W. K.; Mater. Lett. 1984, 3, 17

c. M. J. Bedzyk, D. Bilderback, J. H. White, H. D. Abruña, G. M. Bommarito, J. Phys. Chem. 90, 4926 (1986)

d. M.J. Bedzyk, D.H. Bilderback, G.M. Bommarito, M. Caffrey, J.S. Schildkraut, Science, 1988, 241, 1788.

15 a. Bedzyk, M. J.; Bommarito, G. M.; Schildkraut, J. S.; Phys. Rev. Lett.,1989, 62, 1376

b. Bedzyk, M.J.; Bommarito, G.M.; Caffrey, M.; Penner, T.L.; Science, 1990, 248, 52

16 a. James, R.W.; The Optical Principles of the Diffraction of X-rays," Oxbow Press, Woodbridge, Connecticut, 1982.

b. see also: Bilderback, D.H.; SPIE Proc.1982, Vol. 315, 90

17 Parratt, L.G.; Phys. Rev.,1954, 95, 359

18 Bommarito, G.M.; M.S. Thesis, Cornell University, 1987.

19 Bedzyk, M.J.; Shen,Q.; Keeffe, M.E.; Navrotski, G.; Surface Sci.,1989, 220, 419.

20 Citrin, P.H.; Eisenberger, P; Rowe, J.E.; Phys. Rev. Lett., 1982, 48, 802.

21 a. Felter, T. E.; Hubbard, A. T.; J. Electroanal. Chen. 1979, 100, 473

b. Garwood, G. A.; Hubbard, A. T.; Surf. Sci. 1980, 92, 617

22 a. Osteryoung, R. A.; Anal. Chem. 1963, 35, 1100

b. Osteryoung, R. A.; Anson, F. C.; Anal. Chem. 1964, 36, 975

c. Bagotzky, V. S.; Vasilyev, Yu. B.; Weber, J.; Pirtskhalava, J. N.; J. Electroanal. Chem. 1970, 27, 31

d. Novak, D. M.; Conway, B. E.; J. Chem. Soc. Farad. Trans. 1981, 77, 2341

23 White, J. H.; Abruña, H. D.; J. Phys. Chem.,1988, 92, 7131

24 Lu, F.; Salaita, G. N.; Baltruschat, H.; Hubbard, A.T.; J. Electroanal. Chem.,1987, 222, 305

25 Delahay, P. "Double Layer and Electrode Kinetics", Wiley-Interscience, New York, 1965

26 a. Marra, W.C.; Eisenberger, P.; Chou, A.Y.; J. Appl. Phys., 1979, 50, 6927.

b. Becker, R.S.; Golovchenko, J.A.; Patel, J.R.; Phys. Rev. Lett. 1983, 50, 153.

c. Bloch, J.M.; et al; Phys. Rev. Lett., 1988, 61, 2941.

Figure Captions

Figure 1 Generation of a standing wave by the superposition of two coherently related travelling plane waves of the same wavelength. The difference in A and B is the angle of intersection (2θ). At the smaller angle (B) the period of the standing wave is larger.

Figure 2A Illustration of the x-ray standing wave generated by the interference of the coherently related incident and reflected plane waves above a reflecting surface.

Figure 2B Depiction of a generic reflectivity profile in the total external reflection and Bragg regions.

Figure 3 A. Angular dependence of the reflectivity and relative phase as the angle of incidence is scanned across a Bragg reflection.

B. Depiction of the movement of the electric field intensity of a standing wave as the angle of incidence is scanned across a Bragg reflection.

Figure 4 Angular dependence of the reflectivity and the electric field intensity at various positions with respect to the diffraction planes.

Figure 5a Angular dependence (normalized angle scale) of the reflectivity (R) and the relative phase (v) for the specularly reflected plane wave.

Figure 5b Angular dependence of the E-field intensity at Z=0 and $Z=2D_C$ for $|E_0| = 1$.

Figure 6 The experimental arrangement used in x-ray standing wave experiments.

Figure 7 I/Ge(111) bulk-like surface model, showing I atoms covalently bonded along the (111) direction to Ge surface atoms with a SEXAFS determined I-Ge bond length of d_{GeI}= 2.50 Å. The d-spacing for the Ge(111) diffraction planes is d_{111}=3.266 Å. The XSW measured position of ϕ_C= 0.87 places the I atom layer at a distance Δd_I=2.86Å above the Ge(111) bulk-extrapolated surface symmetry plane. Therefore the top Ge surface atom layer is at Δd_{Ge1}= 0.36 Å above this bulk-extrapolated surface symmetry plane.

Figure 8 Experimental data and theoretical curves for the normalized I_{L3} photoelectron yield and Ge(111) reflectivity (R) versus Bragg reflection angle. The upper I_{L3} yield (offset for clarity) was taken from the "as deposited" 1.5 ML I/Ge(111) surface. The lower I_{L3} yield, which shows a stronger modulation amplitude, was taken from the annealed 1 ML I/Ge(111) surface.

Figure 9 A. Schematic of the model used to describe the iodide distribution formed at the electrode surface.

B-D. The theoretical angular dependence of the I_L fluorescence yield for a distribution consisting of: (B) only an ad-layer of varying thickness, (C) an ad-layer 6Å thick, a diffuse layer with a fixed decay length k and a varying initial concentration, (D) an ad-layer 6Å thick, a diffuse layer with a fixed initial concentration but a changing decay length k.

Figure 10 The angular dependence of the experimental I_L fluorescence for the various applied potentials studied and experimental reflectivity at 6.0keV for the polypropylene/solution/Pt/C LSM system.

Figure 11 (a) The angular dependence of the reflectivity at 9.8 keV for the LB film/Au mirror schematically depicted in the inset. (b) The angular dependence of the Zn K_α fluorescence yield at T = 44°C, and (c) at T = 105°C. Inset: Circles represent heavy atoms and vertical line segments represent hydrocarbon chains. The LB bilayers are zinc arachidate (ZnA), ω-tricosanoic acid (ωTA), and cadmium arachidate (CdA). A layer of octadecyl thiol (ODT) was adsorbed onto the gold surface to make it uniformly hydrophobic for the subsequent LB deposition.

A

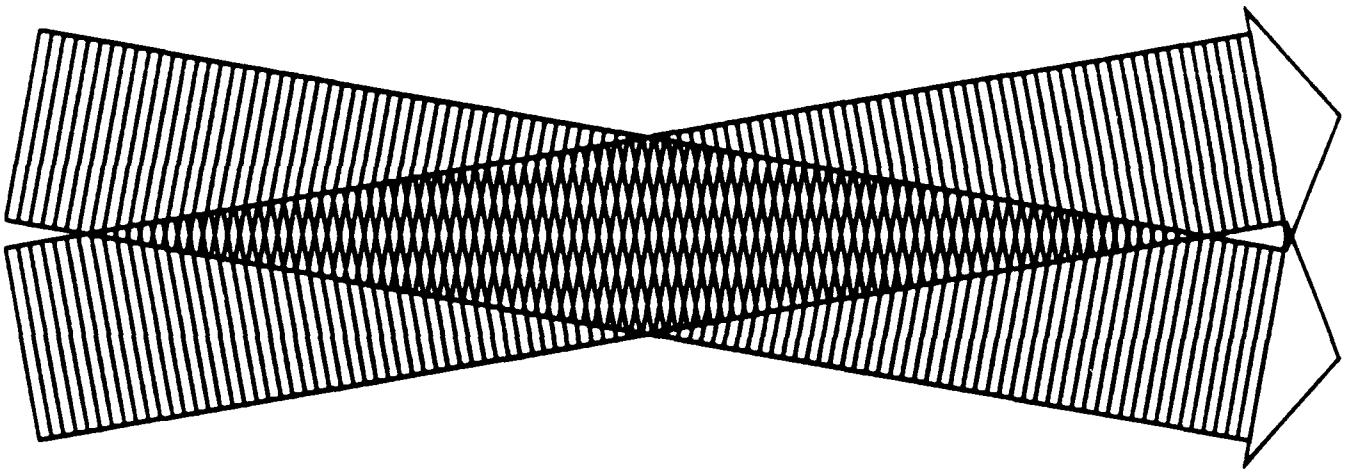

B

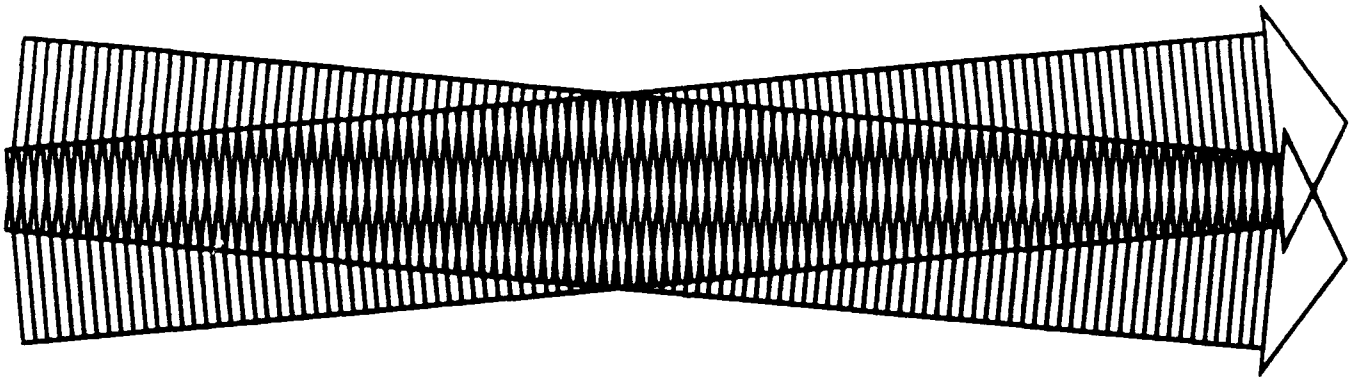

Figure 1

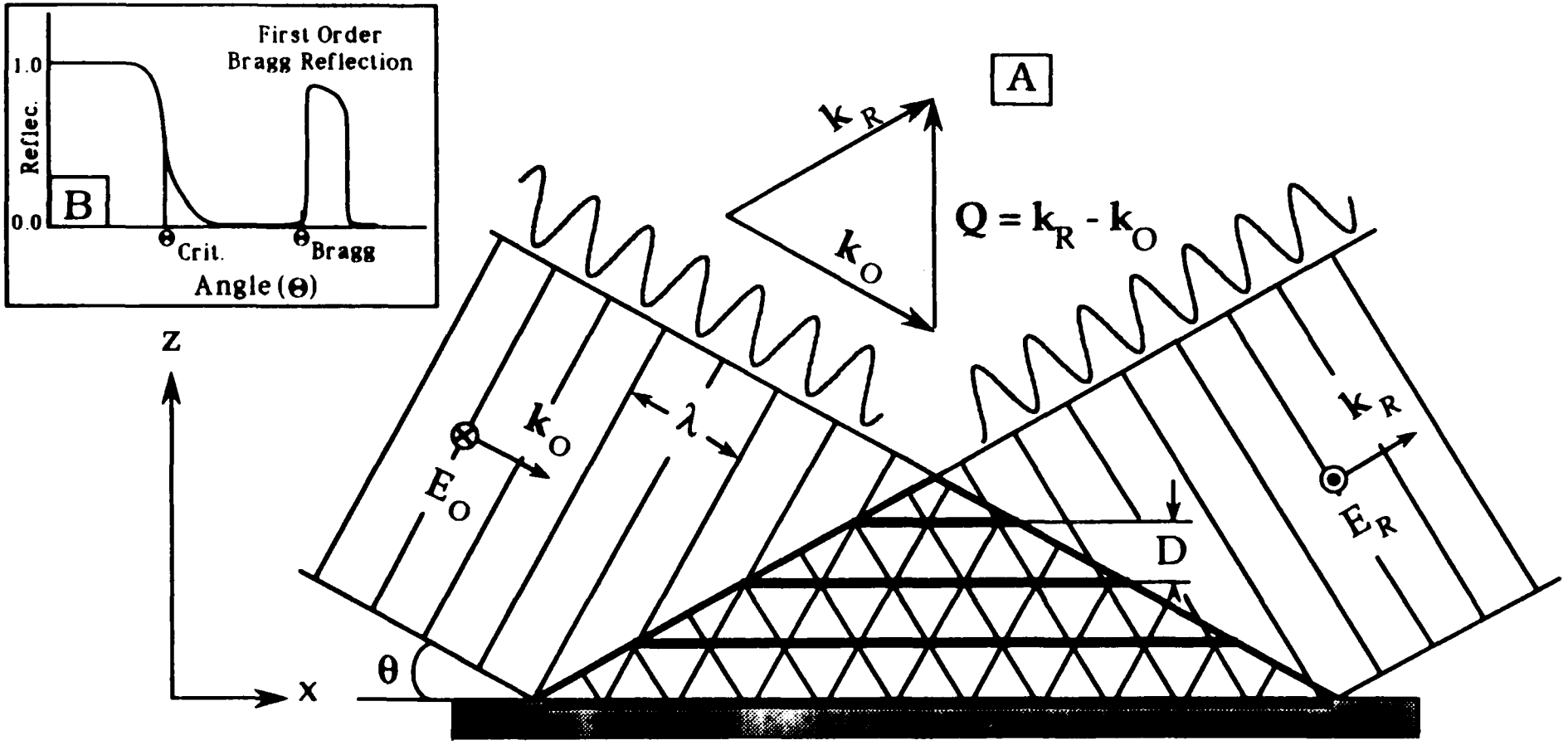
First Order
Bragg Reflection
1.0
Reflec.
0.0
B
θ Crit.
θ Bragg
Angle (θ)
A
k R
k O
Q = k R - k O
Z
X
k O
λ
E O
θ
D
k R
E R

Figure 2

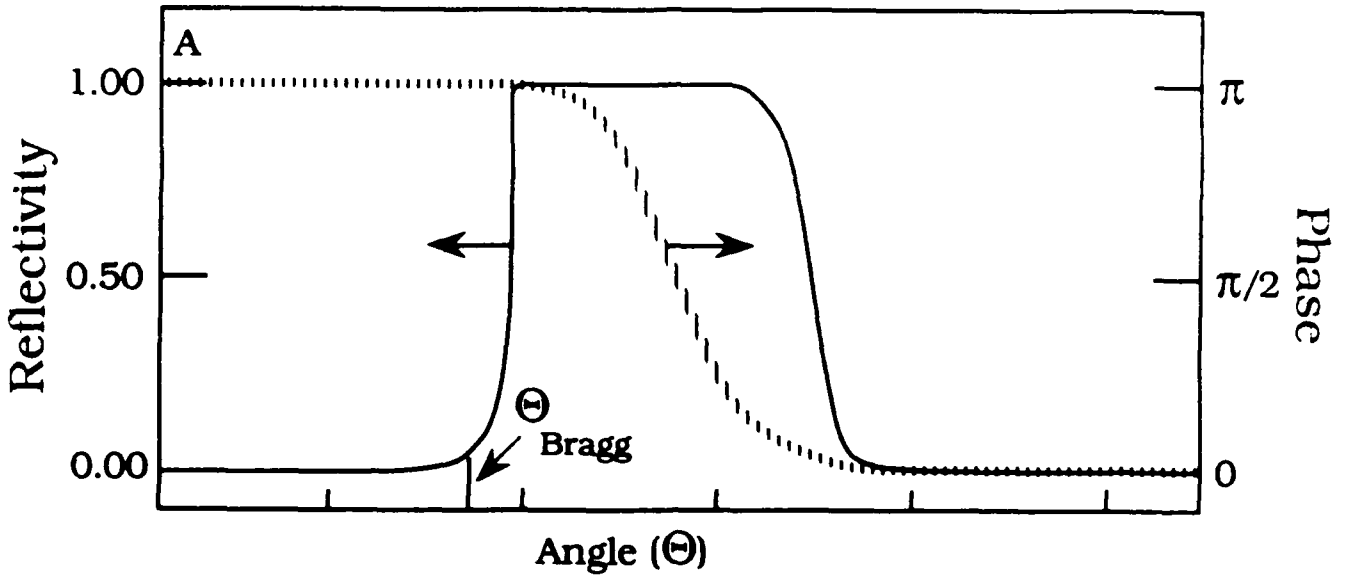
A
1.00
0.50
0.00
Reflectivity
π
π/2
0
Phase
Θ
Bragg
Angle (Θ)

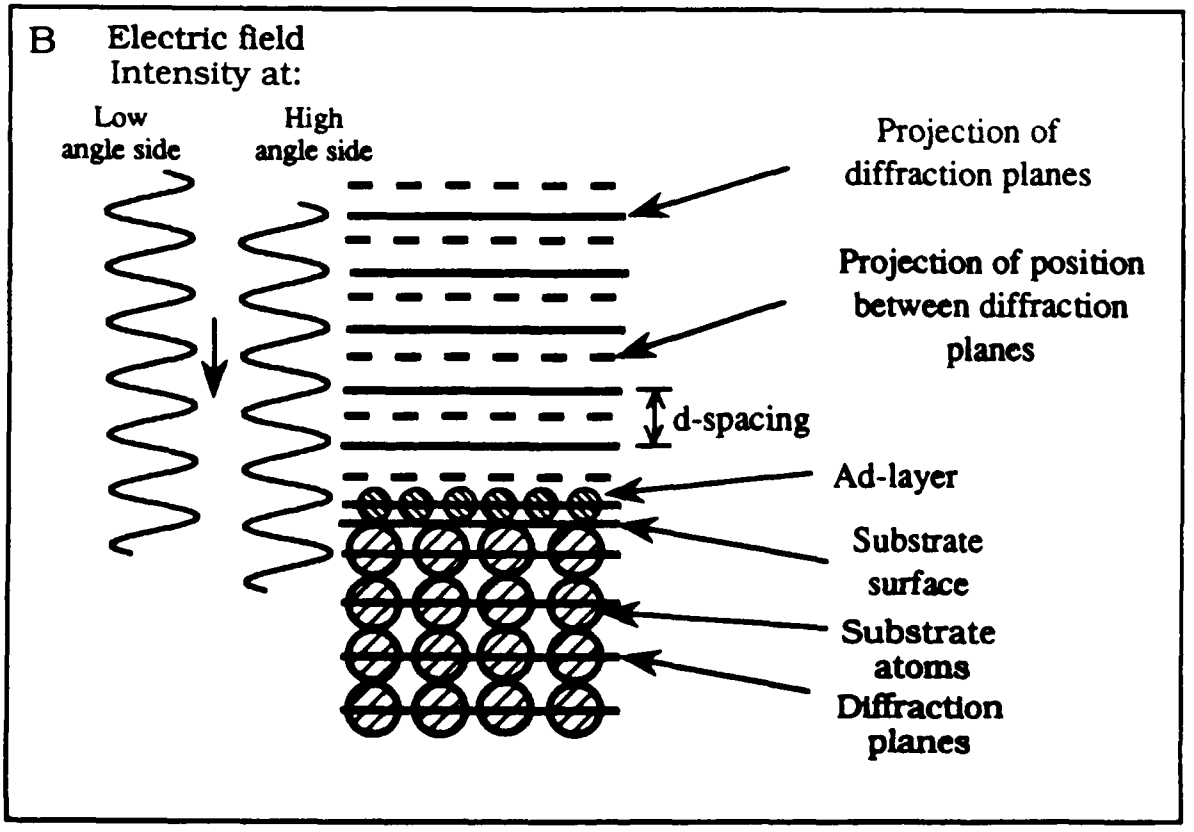
B
Electric field
Intensity at:
Low
angle side
High
angle side
Projection of
diffraction planes
Projection of position
between diffraction
planes
d-spacing
Ad-layer
Substrate
surface
Substrate
atoms
Diffraction
planes

Figure 3

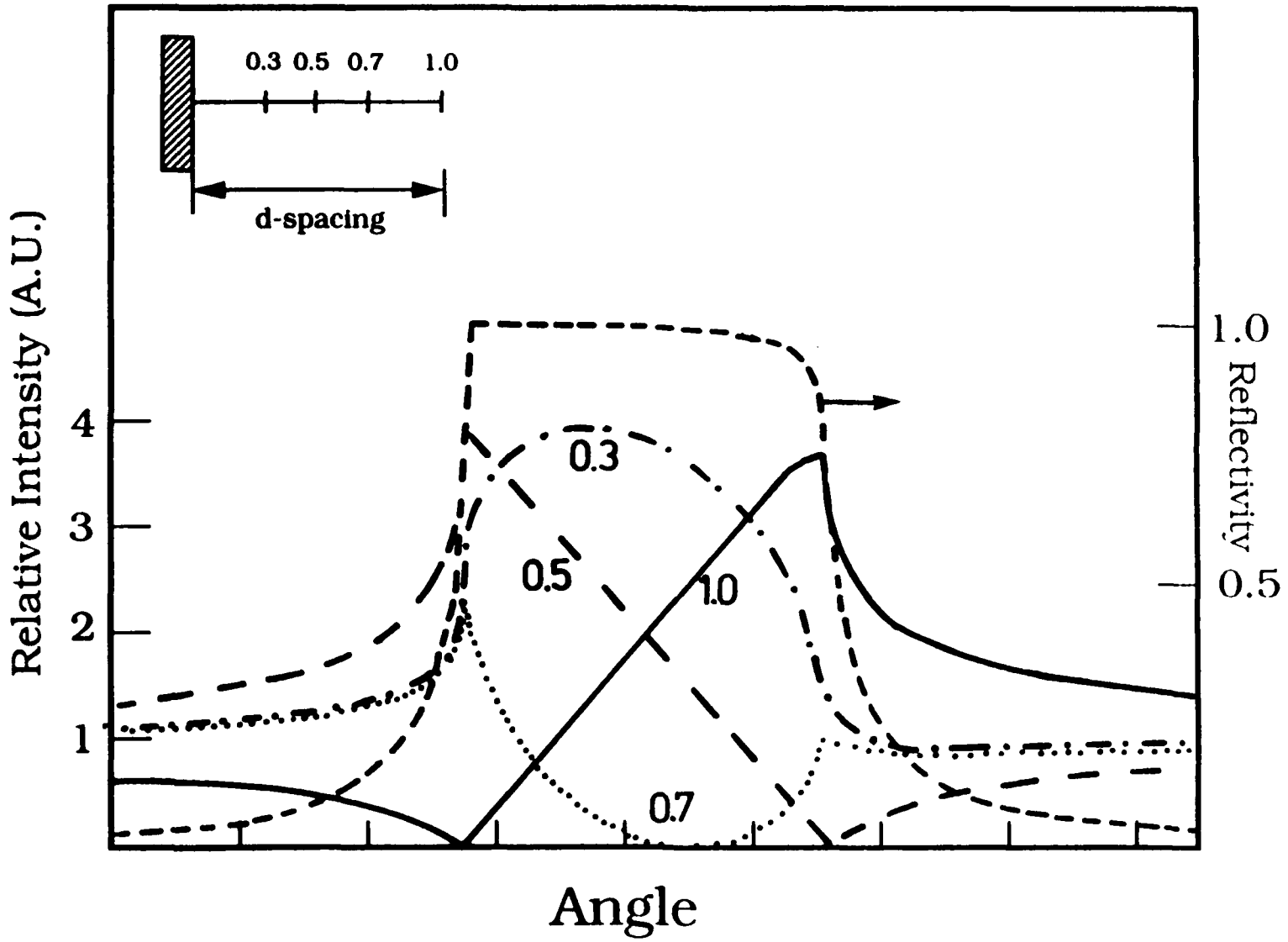
0.3 0.5 0.7 1.0
d-spacing
Relative Intensity (A.U.)
4
3
2
1
0.3
0.5
1.0
0.7
1.0
0.5
Reflectivity
Angle

Figure 4

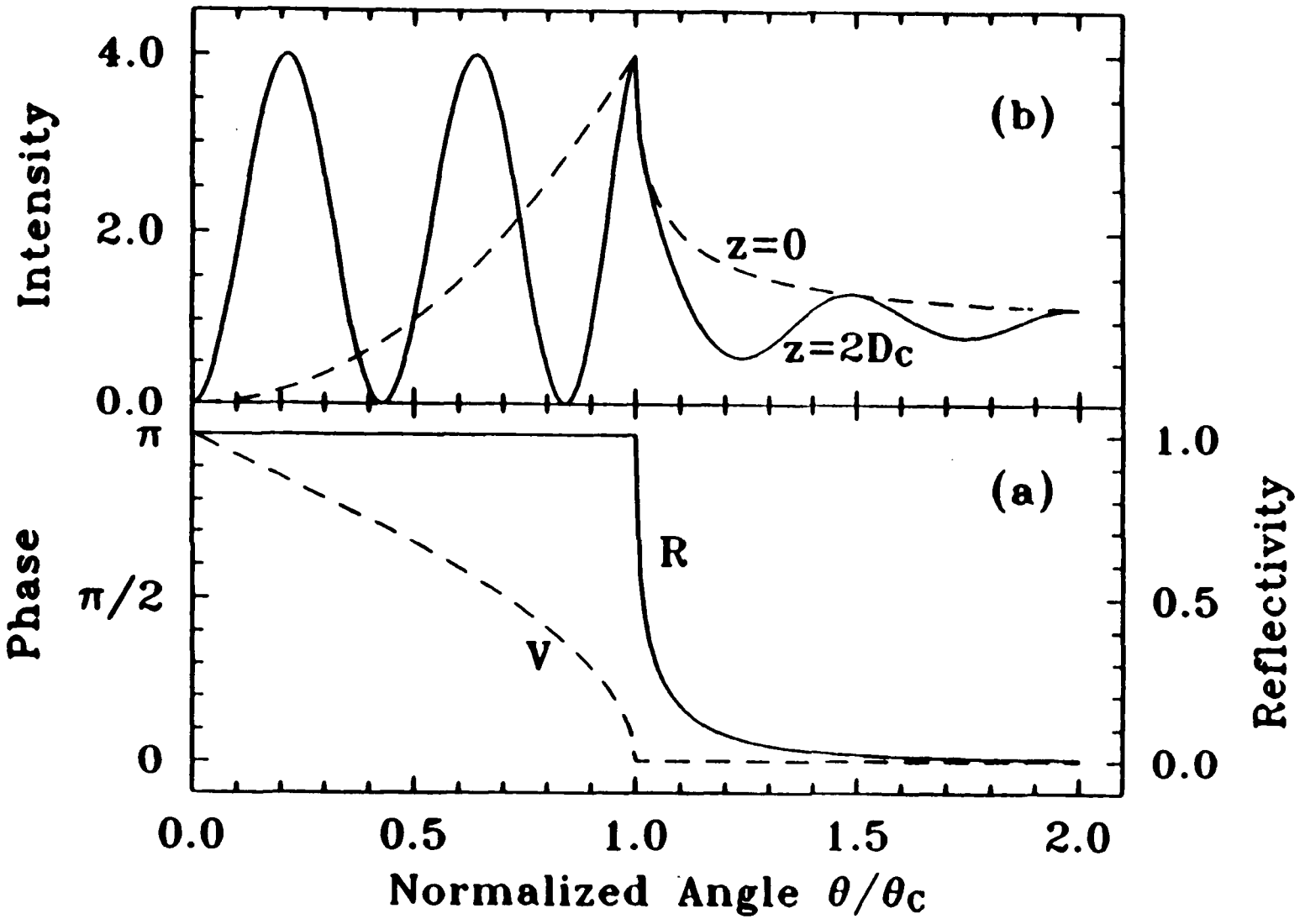
4.0
2.0
0.0
Intensity
(b)
z=0
z=2Dc
π
π/2
0
Phase
(a)
R
V
1.0
0.5
0.0
Reflectivity
0.0
0.5
1.0
1.5
2.0
Normalized Angle θ/θc

Figure 5

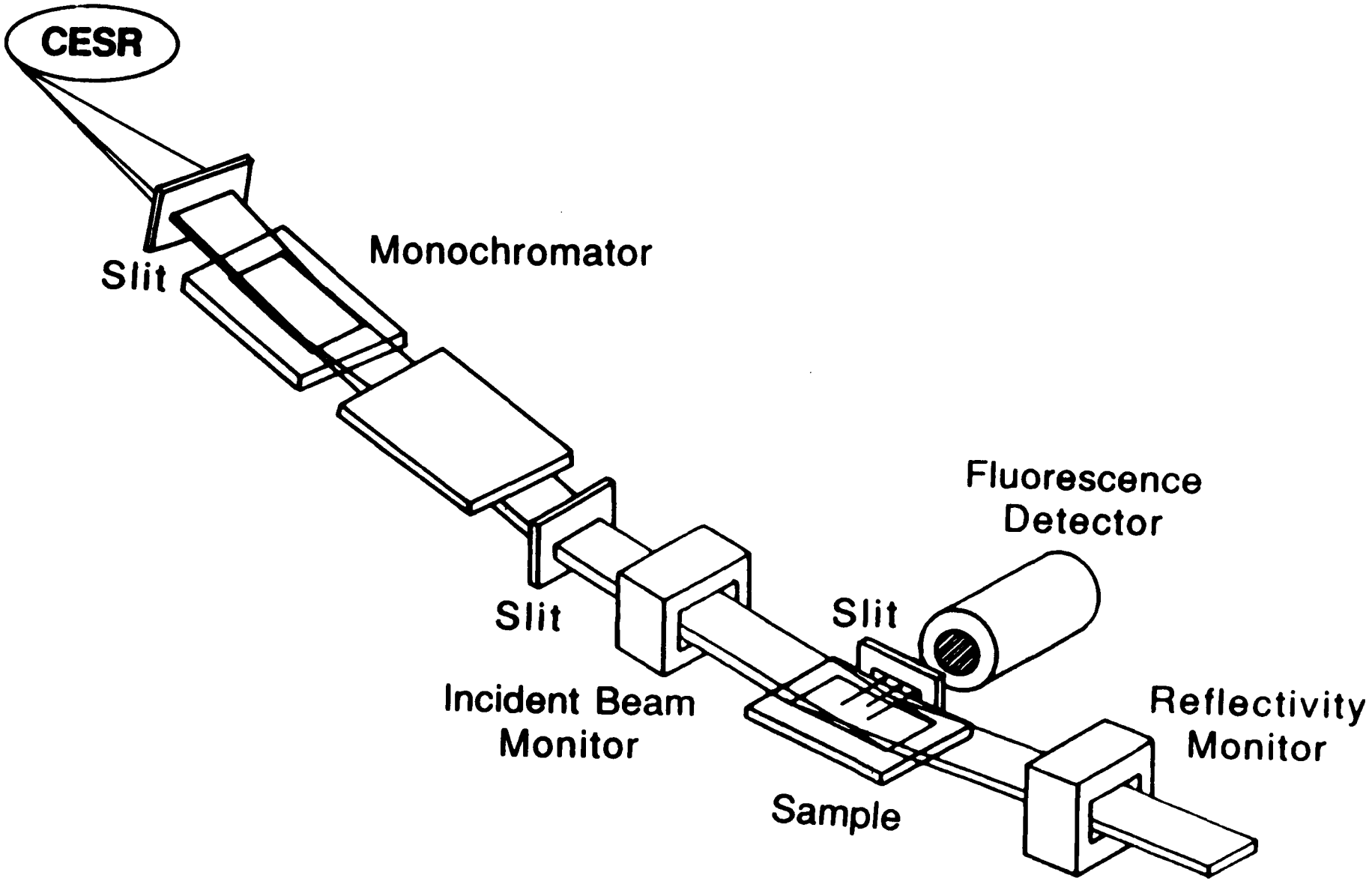
CESR
Slit
Monochromator
Slit
Incident Beam
Monitor
Fluorescence
Detector
Slit
Sample
Reflectivity
Monitor

Figure 6

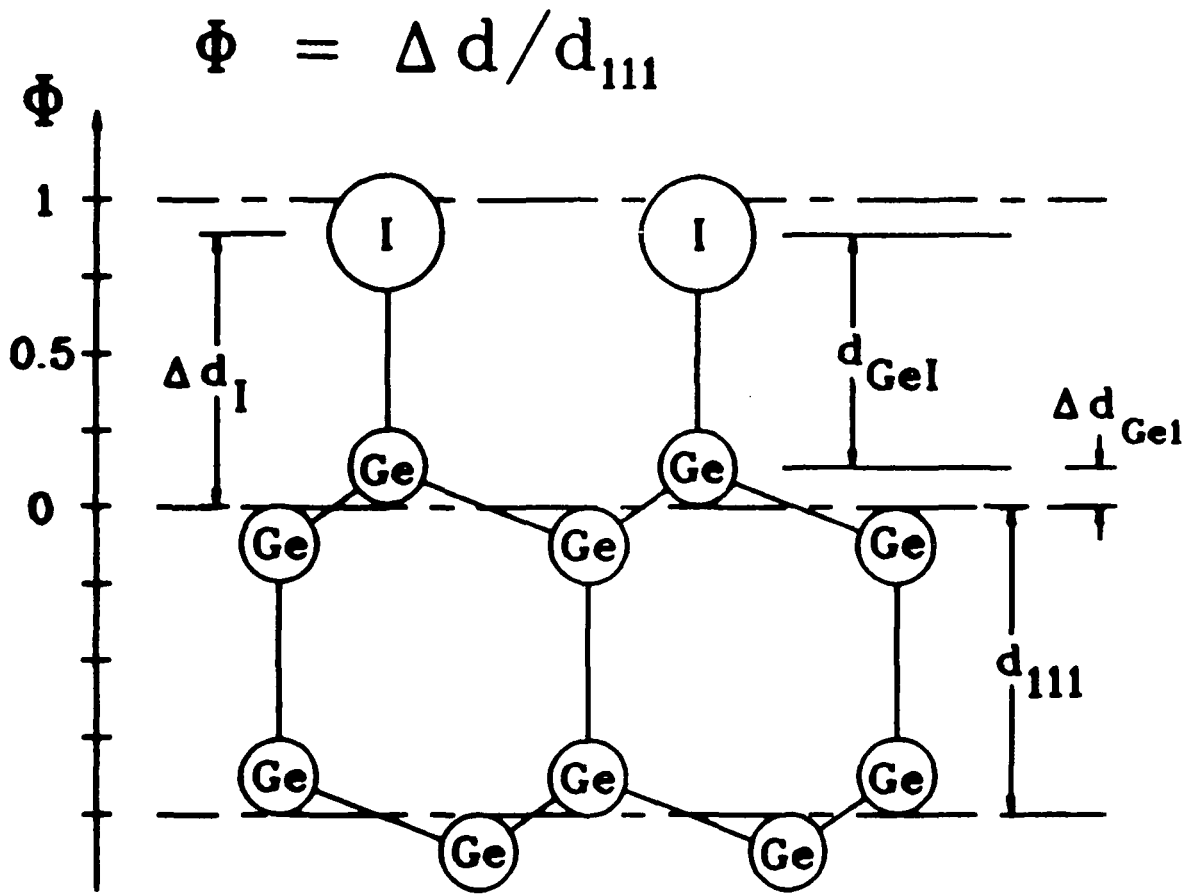
$\Phi = \Delta d/d_{111}$
Φ
1
0.5
0
Δ d_I
I
I
d_GeI
Δ d_GeI
Ge
Ge
Ge
Ge
Ge
Ge
Ge
Ge
Ge
d_111

Figure 7

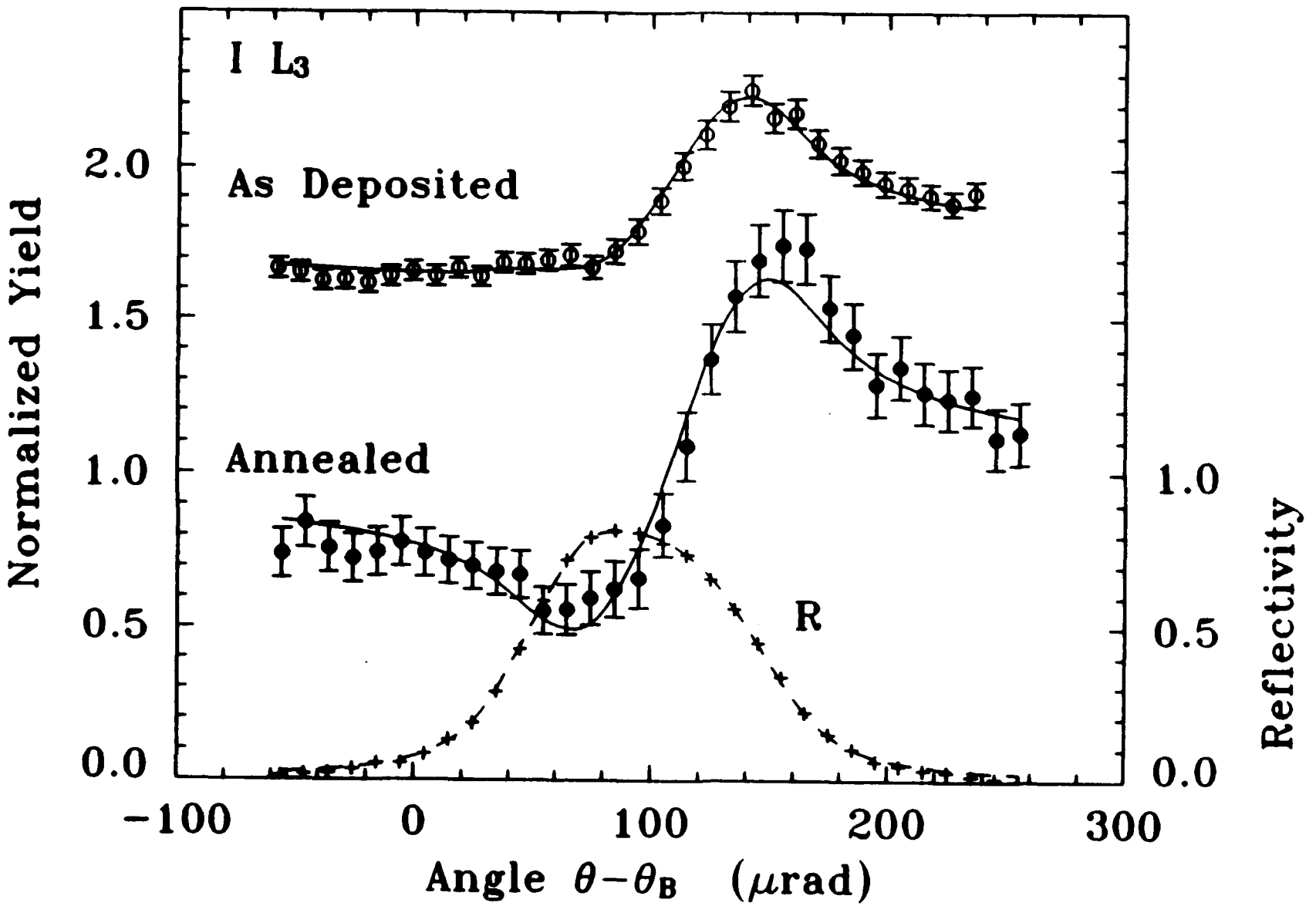
I L3
As Deposited
Annealed
R
Normalized Yield
Reflectivity
2.0
1.5
1.0
0.5
0.0
1.0
0.5
0.0
−100
0
100
200
300
Angle θ−θB (μrad)

Figure 8

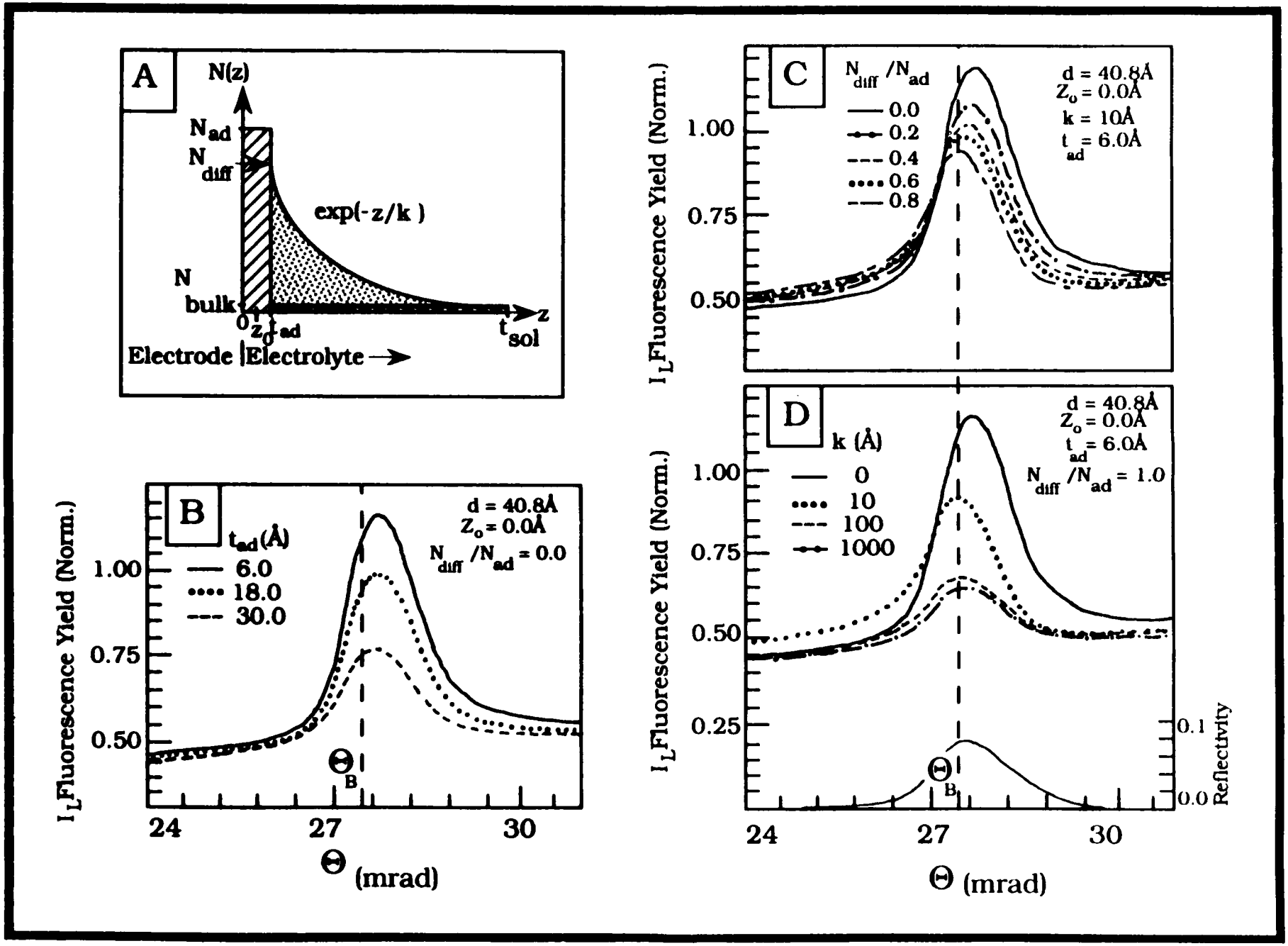
A
N(z)
N_ad
N_diff
exp(-z/k)
N bulk
0
z_0
t_ad
t_sol
z
Electrode | Electrolyte
B
t_ad (Å)
6.0
18.0
30.0
d = 40.8Å
Z_o = 0.0Å
N_diff /N_ad = 0.0
I_L Fluorescence Yield (Norm.)
1.00
0.75
0.50
24
27
30
Θ_B
Θ (mrad)
C
N_diff /N_ad
0.0
0.2
0.4
0.6
0.8
d = 40.8Å
Z_o = 0.0Å
k = 10Å
t_ad = 6.0Å
D
k (Å)
0
10
100
1000
d = 40.8Å
Z_o = 0.0Å
t_ad = 6.0Å
N_diff /N_ad = 1.0
0.25
0.1
0.0
Reflectivity

Figure 9

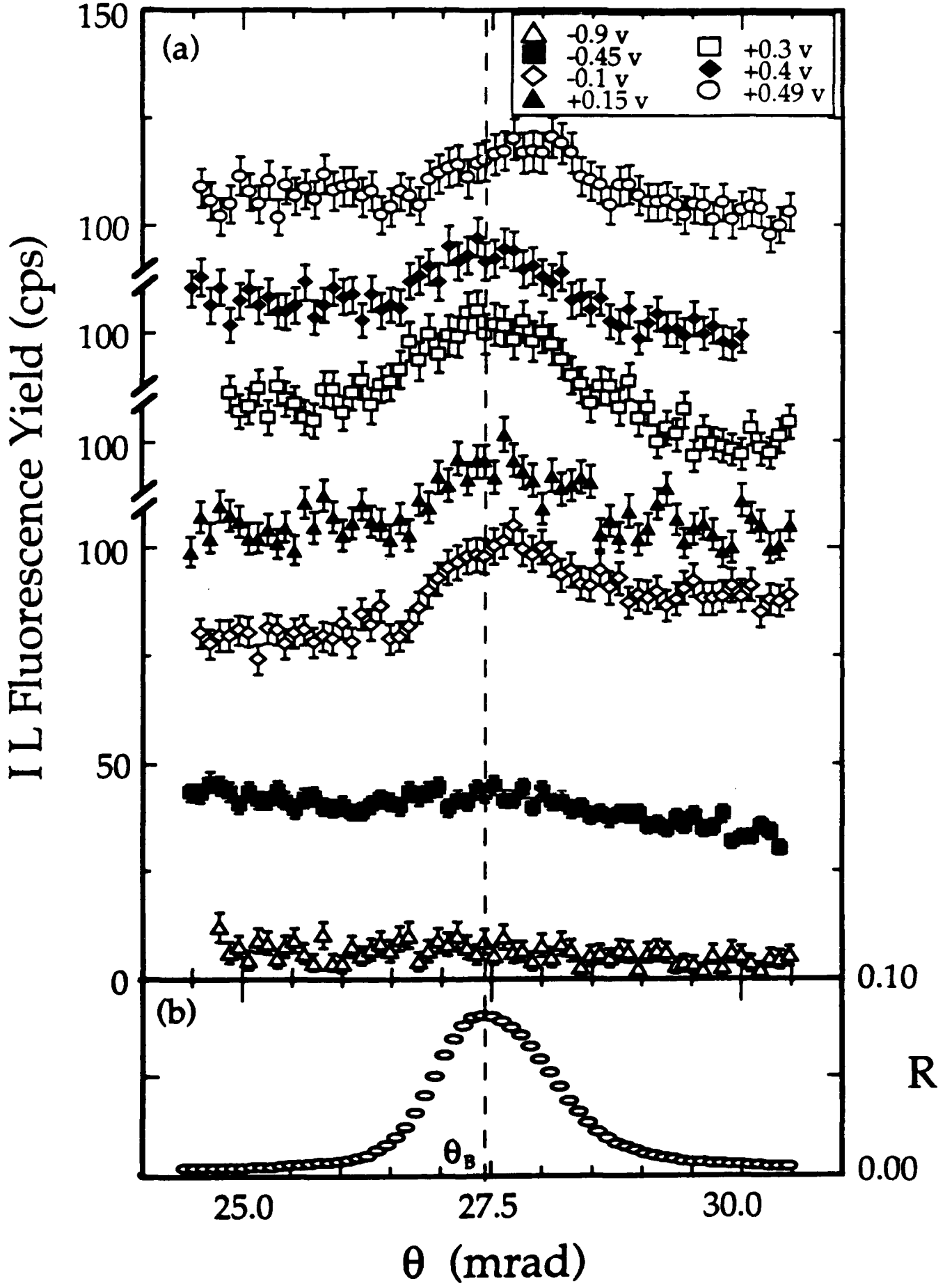
(a)
-0.9 v
-0.45 v
-0.1 v
+0.15 v
+0.3 v
+0.4 v
+0.49 v
150
100
100
100
50
0
I L Fluorescence Yield (cps)
(b)
0.10
0.00
R
θB
25.0
27.5
30.0
θ (mrad)

Figure 10

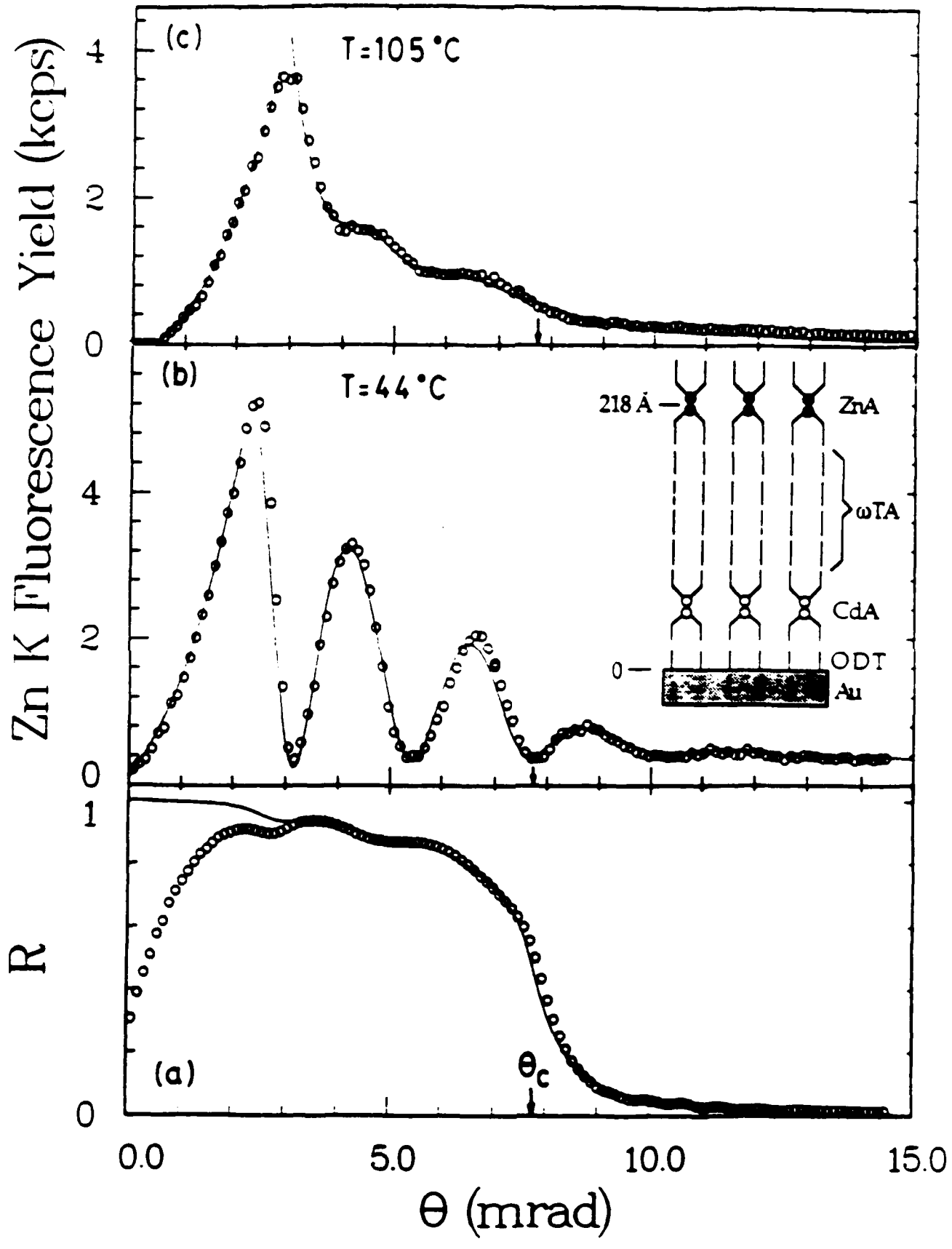
(c)
T=105 °C
(b)
T=44 °C
218 Å
ZnA
ωTA
CdA
ODT
Au
(a)
θ_c
Zn K Fluorescence Yield (kcps)
R
0.0
5.0
10.0
15.0
θ (mrad)

Figure 11

Table I. Parameters from Analysis of I L Fluorescence Yields

Potential (V, vs Ag/AgCL)	Normalized Off-Bragg Yield	Normalized Background Slope	Angular Position of Fluorescence Peak (mrad)	Modulation Amplitude (% of Off-Bragg)
-0.90	0.07 ± 0.04	-0.036 ± 0.005	-	-
-0.45	0.42 ± 0.02	-0.040 ± 0.003	-	-
-0.10	1.0 ± 0.03	+0.025 ± 0.001	27.88 ± 0.06	20 ± 1
0.15	1.38 ± 0.03	-0.001 ± 0.001	27.78 ± 0.06	16 ± 1
0.30	1.20 ± 0.04	-0.016 ± 0.001	27.58 ± 0.06	25 ± 1
0.40	1.37 ± 0.04	-0.017 ± 0.001	27.48 ± 0.06	15 ± 1
0.49	1.44 ± 0.03	-0.009 ± 0.001	27.98 ± 0.06	16 ± 1

The background slope for a random distribution is -0.037
The off-Bragg yield was corrected for variations in the solution layer thickness with potential

Table II. Model Parameters Determined by Non-linear Least Square Fitting of the I L Fluorescence Yield Profiles

Potential (V, vs Ag/AgCl)	Ad-Layer Thickness t(ad) (Å)	Fractional Concentration N(diff)/N(ad)	Diffuse Layer Decay Length k (Å)	Normalized Ad-layer Coverage
-0.90	-	-	-	0.07 ± 0.04
-0.45	-	-	-	0.42 ± 0.02
-0.10	10.0 ± 1.7	0.095 ± 0.005	50 ± 7	1.00 ± 0.02
0.15	10.5 ± 1.8	0.039 ± 0.003	115 ± 18	1.26 ± 0.02
0.30	11.4 ± 2.0	0.0081 ± 0.0021	588 ± 80	1.19 ± 0.03
0.40	10.3 ± 1.6	0.0053 ± 0.0016	824 ± 123	1.25 ± 0.02
0.49	10.8 ± 1.8	0.020 ± 0.002	214 ± 35	1.32 ± 0.02
The thickness of the topmost Pt layer in the LSM was determined to be 16.0 ±0.5 Å				

Table III

X-ray Standing Wave Measured Values of the Zn^{+2} Excess Surface Concentration, N_C and Debye length L' as a Function of pH.*

pH	N_C(M)	L'(Å)
6.8	0.31±0.04	58±4
4.4	0.31±0.02	8±2
2.0	0.18±0.02	3±1

*Bulk Zn^{+2} concentration was 0.1mM